Remote Sens. **2015**, *7*, 13606-13625; doi:10.3390/rs71013606

OPEN ACCESS

remote sensing

ISSN 2072-4292

www.mdpi.com/journal/remotesensing

Article

Estimating the Augmented Reflectance Ratio of the Ocean Surface When Whitecaps Appear

Zhantang Xu [1], Wen Zhou [1], Zhaohua Sun [1,*], Yuezhong Yang [1], Junfang Lin [1], Guifen Wang [1], Wenxi Cao [1] and Qian Yang [2]

[1] State Key Laboratory of Tropical Oceanography, South China Sea Institute of Oceanology, Chinese Academy of Sciences, Guangzhou 510301, China; E-Mails: xujiantang@163.com (Z.X.); wenzhou@scsio.ac.cn (W.Z.); wuli@scsio.ac.cn (Y.Y.); linjunfang301@163.com (J.L.); guifenwang@scsio.ac.cn (G.W.); wxcao@scsio.ac.cn (W.C.)

[2] Institute of Oceanographic Instrumentation, Shandong Academy of Sciences, Qingdao 266001, China; E-Mail: qian.yang@ymail.com

***** Author to whom correspondence should be addressed; E-Mail: joeysun@scsio.ac.cn; Tel./Fax: +86-020-8902-3167.

Academic Editors: Raphael M. Kudela, Xiaofeng Li and Prasad S. Thenkabail

Received: 3 August 2015 / Accepted: 8 October 2015 / Published: 20 October 2015

Abstract: The presence of foam influences the accuracy of satellite-derived water-leaving radiance. A model has been developed to estimate the augmented reflectance ratio ($A(\lambda, U)$) due to differences in the fraction of whitecap coverage (w) on the ocean surface. $A(\lambda, U)$ can be calculated from the product of w and $\rho(\lambda, U)$, where $\rho(\lambda, U)$ is the augmented ratio of the reflectance of background water ($R_b(\lambda)$) caused by the presence of whitecaps. Our results showed that the average $A(400\sim700, U)$ in the visible region was approximately 1.3% at U = 9 m·s^{-1}, 2.2% at U = 10 m·s^{-1}, 4.4% at U = 12 m·s^{-1}, 7.4% at U = 14 m·s^{-1}, 19% at U = 19 m·s^{-1} and 37.9% at U = 24 m·s^{-1}, making it is necessary to consider the augmented reflectance ratio for remote sensing applications. By estimating remote sensing augmented reflectance using $A(\lambda, U)$, it was found that the result was in good agreement with previous studies conducted in other areas with U from 9 to 12 m·s^{-1}. Since $R_b(\lambda)$ is temporally and spatially variable, our model considered the variation of $R_b(\lambda)$, whereas existing models have assumed that $R_b(\lambda)$ is constant. Therefore, the proposed model is more suitable for estimating the augmented reflectance ratio due to whitecaps.

Keywords: whitecaps; wind speed; remote sensing reflectance; augmented ratio

1. Introduction

The presence of foam at the ocean surface should be taken into consideration not only in radiation budget studies (less solar energy absorbed by the ocean, more solar energy reflected back into space), but also in aerosol and ocean color remote sensing from space [1–6]. Since foam on the ocean surface contains many air bubbles and increases upwelling irradiance, the ocean surface no longer provides a negligible background for atmospheric correction [7]. Actually, the additional or augmented spectral upwelling irradiance from whitecaps must be quantified not only at the wavelength used for atmospheric correction, but also at other wavelengths, particularly in the visible region, because spectral information provides a means of determining water content [8,9]. Therefore, in both the visible- and long-wavelength regions, the influence of foam, whitecaps, and streaks on the optical properties of the ocean should be studied.

When whitecaps were first studied, it was thought that the reflectance of the foam would not change with increasing electromagnetic wavelength. They used a wavelength-independent foam reflectance of 50%–100% in conjunction with estimates of fractional coverage to determine the augmentation effect [10,11]. In 1977, Gordon and Jacobs used a radiation-transfer model to demonstrate that for totally reflecting whitecaps, a wind speed increase from 6 to 14 $m \cdot s^{-1}$ would double the local planetary albedo [12]. However, as experimental evidence began to accumulate, researchers found that the assumption that foam reflectance was independent of wavelength was not appropriate. For example, laboratory measurements carried out by Whitlock *et al.* [13] yielded a value of 55% in the visible part of the spectrum for thick foam in clear water and showed that this value diminished with increasing wavelength beyond 800 nm, with decreases of 5% at 850 nm, 10% at 1020 nm, and 50% at 1650 nm. Observations on foams were also conducted *in situ*. In 1996, field reflectance measurements of foam generated by breaking waves in the surf zone indicated that the reflectance decreased by 40% at 870 nm, 50% at 1020 nm, and 95% at 1650 nm relative to the reflectance at 440 nm [2]. Furthermore, to understand the influence of oceanic whitecaps on the global radiation budget, Frouin *et al.* [4] obtained radiative forcing values reaching 0.7 $W \cdot m^{-2}$ in the Indian Ocean during summer. As a result, we found that the above studies were all performed at wavelengths > 700 nm, because their main purpose was to determine the atmospheric correction needed when whitecaps appeared. More recently, the water-leaving radiance in the visible wavelength has been used by researchers to determine seawater contents such as colored dissolved organic matter (CDOM), suspended particulate matter (SPM), chlorophyll a, and particulate organic carbon (POC) [14–16]. Researchers have even used remote sensing data in the visible wavelengths to assess diffuse attenuation coefficients and euphotic depths [17,18]. Therefore, it is important to assess the influence of whitecaps on the radiance received by satellite sensors in the visible wavelengths. Moore *et al.* [8,19] have designed a measurement system to determine the spectral reflectance of whitecaps in the visible wavelengths. During their experiments, however, the remote sensing augmented reflectance results were derived assuming a single constant reflectance of background seawater. Because the reflectance of seawater changes in different ocean regions, the results obtained by Moore *et al.* did not satisfy the needs of global research. Furthermore, since there were only

five wave bands in the visible wavelength during Moore *et al.*'s experiment, a hyperspectral investigation also needs to be conducted for the future research.

In this research, a hyperspectral measurement system has been designed specifically to measure the reflectance of the sea surface, including whitecaps and background water. During the expedition, whitecaps were frequently present at the measurement sites, enabling reflectance values for natural foam to be collected at a wavelength resolution of 1.6 nm. Based on the measured reflectances, a new model suitable for different ocean waters was developed to estimate the augmented reflectance ratio when the surface was covered with whitecaps.

2. Materials and Methods

2.1. Description of the Model

The reflectance of the sea surface can be given by:

$$\mathrm{R}(\lambda) = \frac{L_u(\lambda, \theta, \varphi)}{E_d(\lambda)} \tag{1}$$

where $L_u(\lambda, \theta, \varphi)$ is the upwelling radiance from the sea surface and $E_d(\lambda)$ is the downwelling irradiance above the seawater. When whitecaps appear, the reflection characteristics of the sea surface can be described as:

$$R_t(\lambda, \mathrm{U}) = (1 - w(U))R_b(\lambda) + w(U)R_w(\lambda) \tag{2}$$

where $R_t(\lambda, \mathrm{U})$ is the total reflectance of the sea surface including whitecaps and the whitecap-free surface, $\mathrm{w}(U)$ denotes the fractional coverage of whitecaps, and $(1 - \mathrm{w}(U))$ denotes the fraction of the surface without whitecaps. $R_b(\lambda)$ is the reflectance of the whitecap-free surface, which can be easily obtained because it simply involves measuring the background seawater, and $\mathrm{R_w}(\lambda, \mathrm{U})$ is the weighted average whitecap reflectance. $\mathrm{R_w}(\lambda, \mathrm{U})$ is difficult to obtain because of the varying coverage of whitecaps on the sea surface. As wind increases, the sea surface is roughened by intermediate short gravity waves, which break after reaching a critical steepness. This breaking produces foam patches and bubbly streaks, and finally the sea becomes almost completely covered by a layer of foam [20,21]. When whitecaps occur, it is generally assumed that the sea surface consists of spume, foam streaks, surface foam, bubble clouds, and background sea surface. Air bubbles in seawater substantially scatter incident solar light. Different surface characteristics have different bubble distribution, which leads to different upwelling radiance.

Therefore, the weighted average whitecap reflectance $R_w(\lambda, \mathrm{U})$ was introduced to represent the reflectance for a particular whitecap area (because the reflectance of whitecaps changes at different whitecap positions). $\mathrm{R_w}(\lambda, \mathrm{U})$ is described as

$$\mathrm{R_w}(\lambda, \mathrm{U}) = [1 + \rho(\lambda, \mathrm{U})]\mathrm{R_b}(\lambda) \tag{3}$$

where $\rho(\lambda, \mathrm{U})$ is the augmented ratio of the reflectance of background water (*i.e.*, the augmented reflectance ratio for a particular whitecap area. This parameter is used to describe the discrepancy between the reflectance of a surface with whitecaps and a whitecap-free surface). Then the augmented reflectance ratio for a whitecap-free surface ($\mathrm{A}(\lambda, \mathrm{U})$) (*i.e.*, the augmented reflectance ratio of the whole ocean surface. This parameter is used to describe the discrepancy between the whole surface with no

whitecaps and when whitecaps appear on the surface; it depends on the fractional coverage of whitecaps, as Equation (2) shows) is given by

$$\mathrm{A}(\lambda, \mathrm{U}) = \frac{R_t(\lambda, \mathrm{U}) - R_b(\lambda)}{R_b(\lambda)} \tag{4}$$

Whitecaps are typically related to environmental parameters such as wind speed, wind friction velocity, and the temperature difference between the atmosphere and the sea surface. For the sake of simplicity, it is assumed that whitecaps are related only to wind speed because they are primarily determined by wind speed [8]. Therefore, by combining Equations (2) and (3), Equation (4) is simplified to

$$\mathrm{A}(\lambda, \mathrm{U}) = w(\mathrm{U})\rho(\lambda, \mathrm{U}) \tag{5}$$

where U is the wind speed at 10 m elevation. All the notations used in this study are given in Table 1. A flowchart of the model procedure is shown in Figure 1. As the flowchart shows, $w(\mathrm{U})$ and $\rho(\lambda, \mathrm{U})$ are the primary parameters that must be obtained. The model is based on the data of $R_b(\lambda)$ and $R_x(\lambda)$. Therefore, the first step is to obtain the reflectance of the sea surface, including whitecaps and unbroken seawater *in situ*.

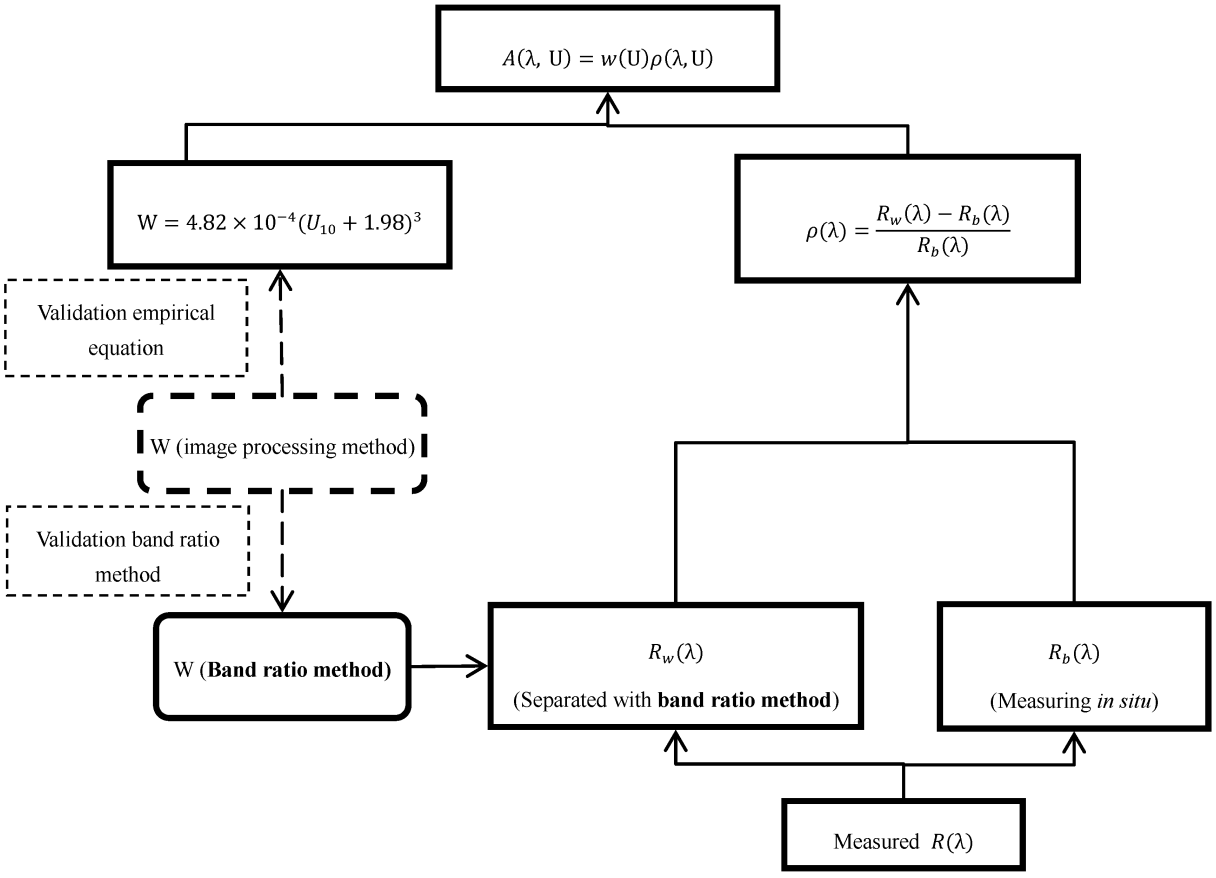

Figure 1. Flowchart of the model process. The dashed lines indicate a standard w to validate the w obtained by the band ratio and empirical methods.

Table 1. Notations used in this paper.

Notation	Description	Unit
$A(\lambda, U)$	augmented ratio of reflectance for the surface	None
$Ed(\lambda)$	downwelling irradiance above the seawater	$\mu W \cdot cm^{-2} \cdot nm^{-1}$
$Lu(\lambda,\theta, \varphi)$	upwelling radiance from sea surface	$\mu W \cdot cm^{-2} sr^{-1} \cdot nm^{-1}$
$L_w(\lambda,\theta,\varphi;\theta_0,\varphi_0)$	water-leaving radiance	$\mu W \cdot cm^{-2} \cdot sr^{-1} \cdot nm^{-1}$
$L_{sky}(\lambda, \theta, \varphi; \theta_0, \varphi_0)$	reflection radiance of incident sky radiance	$\mu W \cdot cm^{-2} sr^{-1} \cdot nm^{-1}$
$R(\lambda)$	reflectance of sea surface including $R_b(\lambda)$ and $R_x(\lambda)$	sr^{-1}
$R_w(\lambda, U)$	the weighted average whitecap reflectance	sr^{-1}
$R_x(\lambda)$	reflectance of whitecaps	sr^{-1}
$R_b(\lambda)$	reflectance of unbroken background seawater	sr^{-1}
U_{10}	wind speed at 10 m elevation	$m \cdot s^{-1}$
$w(U)$	fractional coverage of whitecaps and foam	None
$y(\lambda)$	equal to $\rho(\lambda, U)/\rho(400, U)$	None
$\rho(\lambda, U)$	the augmented ratio of the reflectance of background water	None
ΔT	difference between the temperature of the atmosphere and the sea surface water	℃
λ	wavelength	nm

2.2. A Description for the Observation Instrument

To obtain reflectance values, a whitecap measurement system was designed specifically for this study. A schematic overview of this system is shown in Figure 2a. The system has two hyperspectral spectrometers (Avaspec-2048FT-3-DT, Avantes, The Netherlands) which are connected separately to two kinds of fiber optic detectors. These optical detectors can monitor different light fields simultaneously. Furthermore, a high-definition camera is mounted beside the optical detectors to record simultaneously with the radiometer measurements to provide a visual reference. A lithium battery is used to provide power; it can keep the system working for about 24 hours. The effective integration time ranges from 3 to 3000 ms. In this research, to minimize measurement time, the integration time was set to a constant value, and all the measurements were saved automatically. The system has a wavelength resolution of 1.6 nm. The signal-to-noise ratio for the instrument is 250:1. Optical error is within 0.5% over the 400–700 nm spectral range. All the spectrum graphics given in this paper are for the wavelength range from 400 to 700 nm.

During an observation, the upwelling radiance includes mainly water-leaving radiance $L_w(\lambda, \theta, \varphi; \theta_0, \varphi_0)$ and reflection of incident sky radiance on the seawater surface:

$$L_u(\lambda, \theta, \varphi;\ \theta_0, \varphi_0) = L_w(\lambda, \theta, \varphi;\ \theta_0, \varphi_0) + \sigma \cdot L_{sky}(\lambda, \theta, \varphi;\ \theta_0, \varphi_0) + \Delta \quad (6)$$

where σ is the effective reflection coefficient depending on measurement geometry and wind speed [22], and Δ is the glitter (specular reflection of solar light) and incremental radiance introduced by whitecaps. The error caused by reflection of whitecaps can be ignored when the sea is calm.

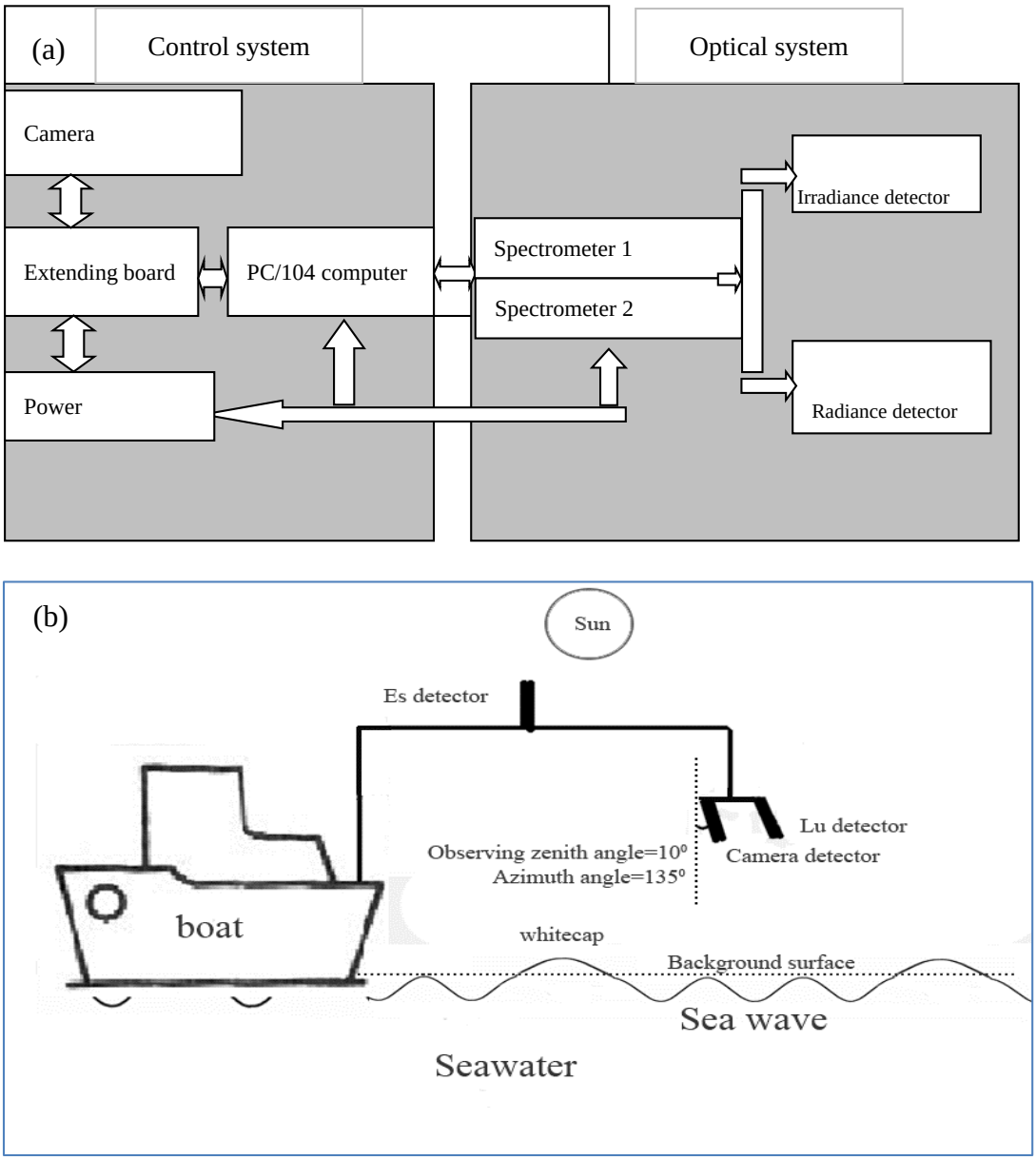

Figure 2. (**a**) Schematic overview of the whitecap measurement system. (**b**) Positions of observation detectors.

As the wind increases, the sea surface becomes complex, and glitter becomes an optical contaminant which must be considered during the observation. Two methods were used to avoid glitter contamination. First, glitter depends on the zenith and azimuth angle of the optical detector and the solar incident radiance. By setting the radiance detector to a suitable zenith and azimuth angle, the effect of glitter can be minimized. The suitable nadir angle for the radiance sensor facing the sea surface has been suggested as 40 °, and the azimuth angle relative to the Sun's azimuth angle has been suggested as 135 °[22]. During the observations in this research, the Sun zenith angle varied from 51 ° to 67 °. The detector was set at a zenith angle of 10° in consideration of the large Sun zenith angle and the complex seawater surface. The azimuth angle was set to values up to 135°. A description of the positions of the observation detectors is shown in Figure 2b. As wind speed increases, the surface geometry becomes complex. This complex surface reflects light in different directions, which somewhat contaminates the

measurements regardless of the observation angle of the detector. Fortunately, the effects on observations of whitecap-free and whitecap-covered surfaces were similar and therefore were not of any significant consequence in determining the spectral variations in whitecap reflectance [2]; second, glitter contamination is also dependent on sky condition. Cloud around the Sun will result in less solar glitter to contaminate measurements. Therefore, in this research, the optical contamination caused by glitter was successfully minimized by setting a suitable observation angle under cloudy sky.

2.3. Observation of Sea Surface Reflectance in situ

Measurement was conducted on the *Shiyan-3* research vessel during a 25-day voyage in the South China Sea in 2012. The reflectance of seawater, sea surface images and videos were all recorded on this cruise. Unfortunately, only four ideal sites were available for the recording to be conducted. In order to analyze the augmented reflectance ratio of the ocean surface when whitecaps appear, more recording of background seawater and whitecap reflectance was required. This was done at another five sites during a 36-day voyage on the *Xinshijian* research vessel in the East China Sea in 2014. During this experiment, all the reflectances were obtained, but no associated image or video data was recorded due to instrument failure. The information for the nine sites is given in Table 2. Clear sky conditions were avoided to eliminate glitter contamination. For safety reasons, the highest wind speed at 10 m elevation was 17.6 $m \cdot s^{-1}$.

Table 2. Description of cloud condition, observation time and wind speed.

Sites	Regions	Time	Sky	Wind Speed ($m \cdot s^{-1}$)
1	South China Sea	30 September 2012	Some clouds	10.9
2	South China Sea	8 October 2012	Overcast	12.8
3	South China Sea	9 October 2012	Overcast	11.7
4	South China Sea	10 October 2012	Overcast	12.2
5	East China Sea	27 November 2014	Some clouds	15.5
6	East China Sea	27 November 2014	Some clouds	10.4
7	East China Sea	28 November 2014	Some clouds	8.6
8	East China Sea	29 November 2014	Some clouds	12.5
9	East China Sea	29 November 2014	Some clouds	17.6

There are large discrepancies in the reflectance spectrums of coastal and ocean seawater [23]. It is clearly more important to study ocean seawater than coastal waters, because it is the primary component of global seawater, occupying about 60% of the global ocean surface [24]. Thus, the purpose of this experiment was to generate a model for estimating the augmented reflectance ratio of ocean seawater. Figure 3 shows the reflectance obtained at nine sites in ocean seawater, in which all the spectral trends are similar in the visible wavelength. At the four sites in the South China Sea research area, the reflectance at 400 nm show little difference: 0.0084 at Site 1, 0.0103 at Site 2, 0.01 at Site 3, and 0.0096 at Site 4. In the East China Sea research region, the reflectance discrepancy was large, with values from 0.0056 to 0.0105, and at Site 7 where the reflectance was largest, with a value of 0.019 at 400 nm. Generally, sites in ocean seawater have similar reflectivity spectrum trends and a large reflectance range, consistent with the present study. Furthermore, the similar sky conditions at all nine sites also met the experimental requirements of this study.

During observations, a camera about 12 m above the sea surface was used to take sea photographs of the sea surface for estimating w using image processing methods. The surface images and the values of $R(\lambda)$, including $R_b(\lambda)$ and $R_x(\lambda)$ in the South China Sea study area are shown in Figure 4.

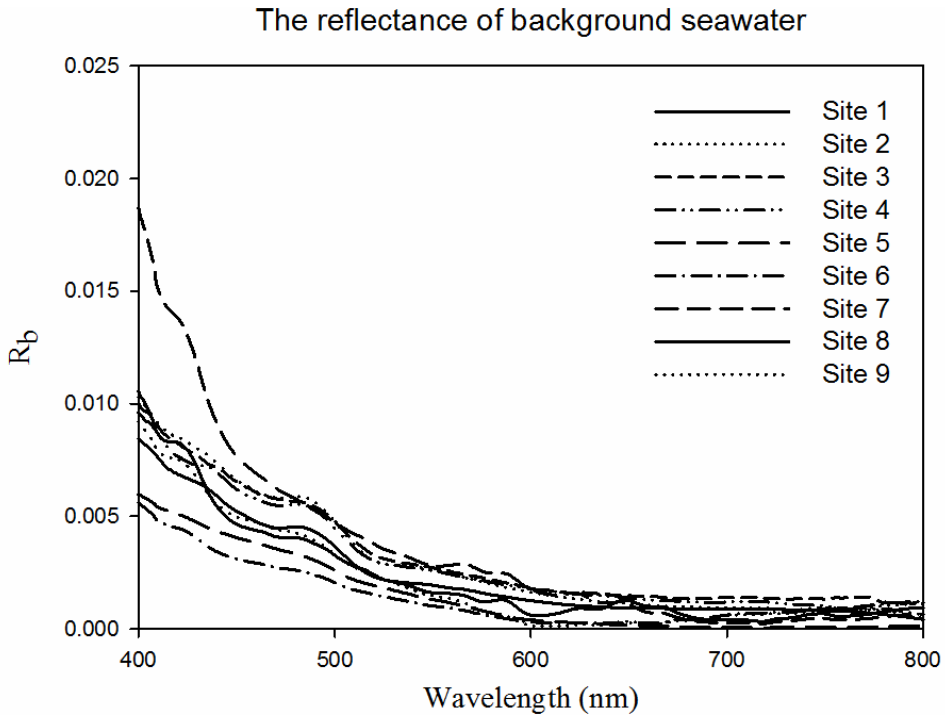

Figure 3. Reflectance of whitecap-free surface at nine sites obtained by measuring the background seawater with the whitecap reflectance measurement instrument.

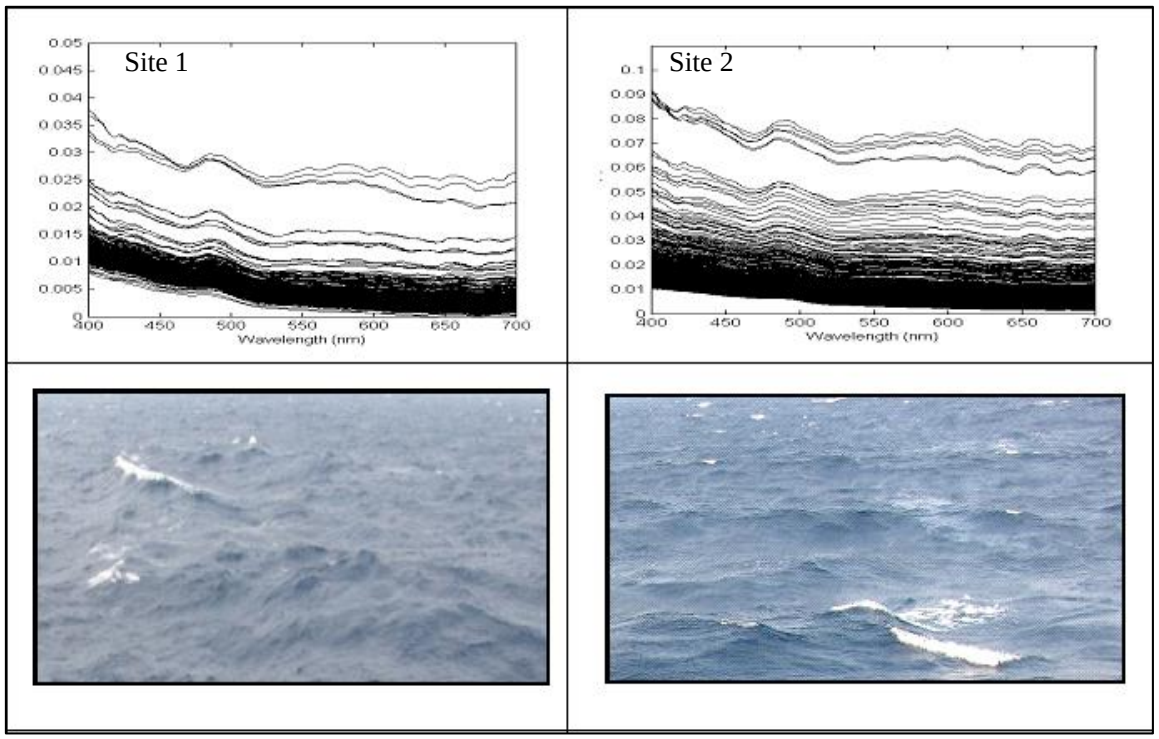

Figure 4. *Cont.*

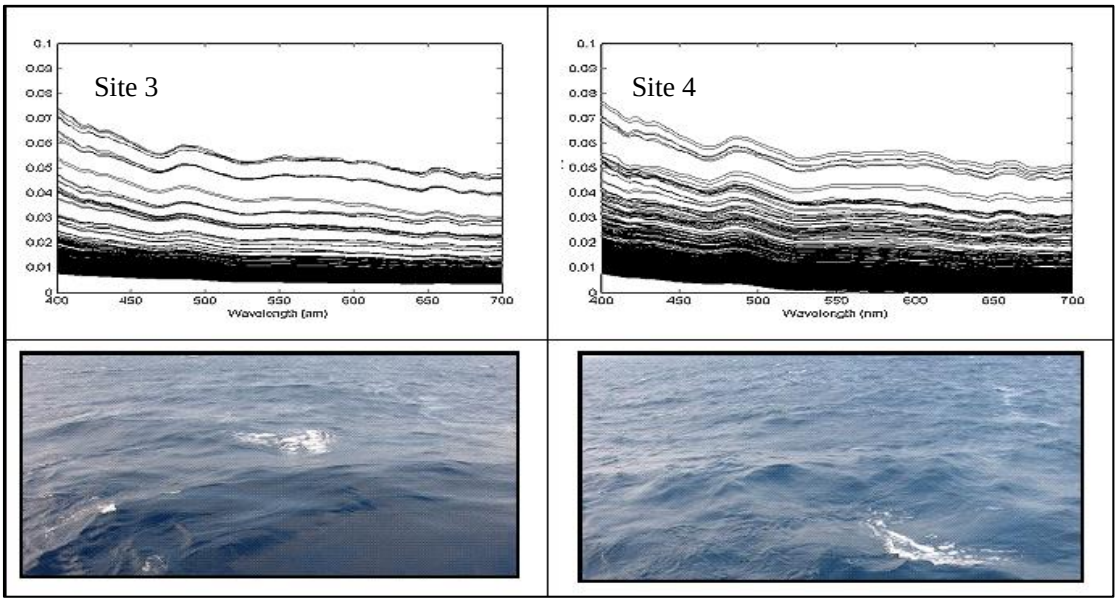

Figure 4. Reflectance spectra at wavelengths from 400 to 700 nm in South China Sea study area. The photographs of the sea surface at each site were used to estimate the fractional coverage of whitecaps using an image processing method.

3. Results

3.1. Calculating the Fractional Coverage of Whitecaps ($w(U)$)

3.1.1. Distinguishing $R_b(\lambda)$ and $R_x(\lambda)$

As shown in the flowchart (Figure 1), $R_b(\lambda)$ and $R_x(\lambda)$ are the required input parameters. $R_b(\lambda)$ has already been obtained, as shown in Figure 3. $R_x(\lambda)$ should be separated from $R(\lambda)$ at each site, and a band ratio method is introduced here.

In most cases, seawater flow velocity and direction ($v(t)$ $\varphi(t)$, where t is the time and φ is the flow direction) change with time. However, $v(t)$ $\varphi(t)$ can be assumed constant when the time is not too long. In this research, $v(t)$ $\varphi(t)$ was fixed because each observation lasted <15 minutes. Then w can be given as

$$\begin{aligned} w &= \frac{v(t)\cdot \emptyset(t)\left(t_w(1)+t_w(2)+t_w(3)+\cdots+t_w(n)\right)}{v(t)\cdot \emptyset(t)\left(\left(t_w(1)+t_w(2)+t_w(3)+\cdots+t_w(n)\right)+\left(t_B(1)+t_B(2)+t_B(3)+\cdots+t_B(n)\right)\right)} \\ &= \frac{\left(t_w(1)+t_w(2)+t_w(3)+\cdots+t_w(n)\right)}{\left(\left(t_w(1)+t_w(2)+t_w(3)+\cdots+t_w(n)\right)+\left(t_B(1)+t_B(2)+t_B(3)+\cdots+t_B(n)\right)\right)} \\ &= \frac{\left(t_w(1)+t_w(2)+t_w(3)+\cdots+t_w(n)\right)}{t_{total}} \end{aligned} \quad (7)$$

where t_W is the appearance time of whitecaps, t_B is the appearance time of unbroken surface, and t_{total} is the total time, which is equal to the sum of t_W and t_B. A schematic diagram for obtaining w was shown in Figure 5. The data sampling rate was 2.9 times per second. Because $t(n)$ is a constant, the recorded data can be used to describe the sampling time. Therefore, Equation 7 can be simplified as

$$w = \frac{numbers(whitecaps)}{numbers(total)} \tag{8}$$

where *numbers(whitecaps)* is the total recorded whitecap times and *numbers(total)* is the total recorded times. To obtain *w*, then, it is necessary to determine whether the recorded spectrum represents $R_b(\lambda)$ or $R_x(\lambda)$. Here, band ratios were used to separate $R_x(\lambda)$ from $R(\lambda)$:

$$\mathrm{B}(\lambda_C, \lambda_D) = \frac{R(\lambda_C)}{R(\lambda_D)} \tag{9}$$

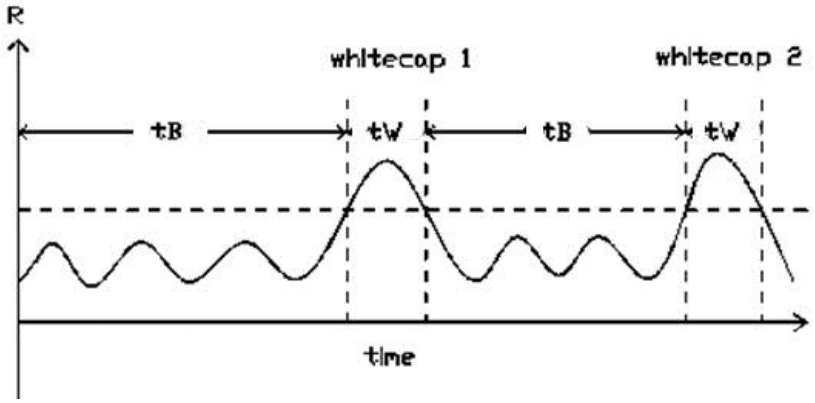

Figure 5. Schematic diagram for estimating the fractional coverage of whitecaps, where t_W is the time during which whitecaps appear and t_B is the time of whitecap-free sea surface.

By comparing $\mathrm{B}(\lambda_C, \lambda_D)$ values at every site, the difference in $\mathrm{B}(\lambda_C, \lambda_D)$ between whitecaps and background seawater may be found. For this purpose, λ_C and λ_D should be determined. If suitable values of λ_C and λ_D are chosen, a larger discrepancy in $\mathrm{B}(\lambda_C, \lambda_D)$ between whitecaps and unbroken background seawater can be obtained.

The important wavelengths for ocean color remote sensing are 412, 443, 490, 520, 555, 620, and 665 nm. Considering that this field work might be extended to the study of ocean color remote sensing, the choice of λ_C and λ_D from these bands is good. By setting λ_C and λ_D as two of these wavelengths, $\mathrm{B}(\lambda_C, \lambda_D)$ was obtained. At every site, all the $\mathrm{B}(\lambda_C, \lambda_D)$ values were sorted in descending order. Generally, larger discontinuities appearing in the ordered lines indicate that more suitable values of λ_C and λ_D have been selected. As a result, it was found that the best value of λ_C was 620 nm and that of λ_D was 412 nm. Figure 6 shows the sorted line of $\mathrm{B}(\lambda_{620}, \lambda_{412})$. Discontinuities occurred at approximately 0.59 at Site 1, 0.71 at Site 2, 0.70 at Site 3, and 0.70 at Site 4. These points can be assumed to be thresholds. Most of the thresholds were close to 0.7 except for Site 1, which had a threshold of approximately 0.59. There was no obvious discrepancy in $R_b(\lambda)$ between Site 1 and the other sites, as shown in Figure 3. The spectral trend of $R_b(\lambda)$ was similar at these sites. The reflectance at Site 1 was only slightly smaller than that at the other sites. Because the observation conditions at these sites were not completely the same, the introduced glitter at Site 1 was somewhat different from that at other sites, which caused a different threshold to be determined at Site 1. However, in this study it was considered that a threshold value of 0.7 ($\mathrm{B}_0(\lambda_{620}, \lambda_{412}) = 0.7$) was reasonable for ocean seawater. All $R_x(\lambda)$ could be separated when $\mathrm{B}(\lambda_{620}, \lambda_{412})$ exceeded the threshold. The instrument incorporated a camera and an

optical radiance detector to observe a single seawater surface location. Comparison between the spectrum and image data showed that the band ratio method effectively separated $R_x(\lambda)$ from $R(\lambda)$.

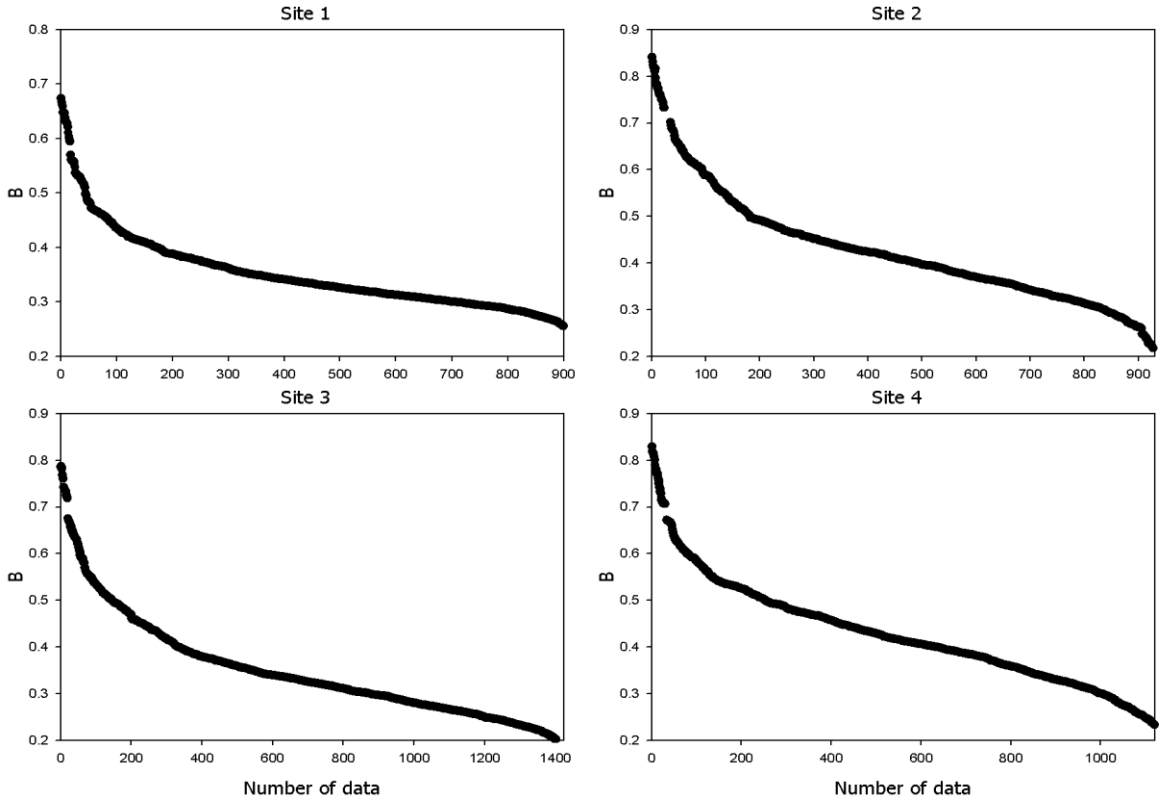

Figure 6. Sorted plots of $B(\lambda_{620}, \lambda_{412})$ at Sites 1, 2, 3 and 4. In most cases, discontinuities in the sorted lines occur close to 0.7.

3.1.2. Validation of the Band Ratio Method and Empirical Equation

By separating $R_x(\lambda)$ from $R(\lambda)$, $w(U)$ was obtained using Equation (8), as shown in Table 3. Image processing is widely used to estimate $w(U)$ [25–29]. During this observation, another camera located at about 12 m above the seawater surface was used to take sea photos. RGB information was then extracted using MATLAB software. R_0, G_0, and B_0 were defined as thresholds. A pixel in the photo was assumed to be a whitecap pixel when its *R*, *G*, and *B* values were larger than the thresholds (R_0, G_0, and B_0). Then *w* can be calculated as $w = Pixel(whitecaps)/Pixel(total)$ where $Pixel(whitecaps)$ is the total number of whitecap pixels and $Pixel(total)$ is the total number of pixels in a photo. Table 3 shows the values of w obtained from photograph processing used to validate the values from band ratio and empirical methods.

A comparison of the values of w obtained using the band ratio and image processing methods shows that the smallest absolute percentage difference is 4.7% at Site 2, and the largest value is as high as 56.1% at Site 4. The mean absolute percentage difference at the four sites is 29.9%. Despite attempts to locate the observation position as far from the vessel as possible, it nevertheless was considered that the hull of the ship may have affected the wave distribution over the sea surface to some extent; if so, this would have affected the accuracy of the w value derived by the band ratio method. However, this result shows that the band ratio method gave a reasonable estimation of w, which is suggested could be used in future remote sensing.

Table 3. Fractional coverage of whitecaps from band ratio, image processing, and empirical equations.

Site	Wind Speed ($m \cdot s^{-1}$)	$B_0(\lambda_{620}, \lambda_{412})$	W (Band Ratio Method)	W (Image Processing)	W (Empirical Formula)
1	10.9	0.59	0.01967	0.0164	0.0103
2	12.8	0.71	0.02688	0.0282	0.0156
3	11.7	0.7	0.01405	0.0101	0.0123
4	12.2	0.69	0.02482	0.0159	0.0137

To estimate $A(\lambda, U)$, as the flow chart shows, a formula is needed to estimate $w(U)$. Because the band ratio method has not been validated by remote sensing, an empirical equation should be introduced to estimate w. The most common w parameterizations take the form of the power law relation between w and U_{10} in the form $W = aU_{10}^{b}$, in which the values of a and b may be derived from a best-fit procedure for a set of observations. The values for a and b vary widely with different locations and conditions. In a review of tabulated examples in the whitecap literature, it was found that b ranges from 2.0 to 5.16, with an average of roughly 3 [30–32]. The term w has also been reported to be related to the cube of the wind speed, given as $W = a(U_{10} + b)^3$ [28,32,33]. Two possible equations are then obtained either for $U_{10} < 11.25$ $m \cdot s^{-1}$, or for $U_{10} > 9.25$ $m \cdot s^{-1}$. Because the wind speed is greater than 9.25 $m \cdot s^{-1}$ at most sites $m \cdot s^{-1}$, the empirical equation that is applicable when $U_{10} > 9.25$ $m \cdot s^{-1}$ was adopted to estimate w in the present work [28]:

$$w = 4.82 \times 10^{-6}(U_{10} + 1.98)^3 \quad (10)$$

In assessing the suitability of Equation (10) for the study area, it was found that the calculated value of w agreed well with the result estimated by the photograph processing method (see Table 3). Almost all of the values of w were consistent with wind speed. The mean absolute percentage difference was 29.4%. The smallest absolute percentage difference was 13.8% at Site 4, and the largest was 44.7% at Site 2. In most cases, the value of w derived from processed images was larger than that estimated by the empirical equation. Since no prior wind-speed data was available for the study areas, a certain response delay was assumed between increase in wind speed and the formation of whitecaps. Furthermore, the photographs did not cover large area of the sea surface; in addition, some w errors were also expected in the image processing method. As a result, Equation (10) was used to estimate w in the proposed model.

3.2. Extraction of $R_w(\lambda)$

As discussed above, whitecap reflectance was extracted from the overall recorded reflectance data by the band ratio method. Finally, the weighted average whitecap reflectance ($R_w(\lambda, U)$) was obtained. Figure 7 shows $R_w(\lambda, U)$ and $R_b(\lambda)$ at sites 1 to 4, in which it is seen that the reflectance decreases with increasing wavelength, decreasing sharply at short wavelengths from 400 to 600 nm, in a similar manner to the reflectance of the background seawater. The decreasing trend in the reflectance of whitecaps differs somewhat from the background seawater at longer wavelengths. To describe the decreasing trend, values of $R_w(\lambda)/R_w(443)$ are listed in Table 4. For example, at Site 1,

$R_w(490)/R_w(443)$ is 0.90, $R_w(520)/R_w(443)$ is 0.59, $R_w(620)/R_w(443)$ is 0.38, and $R_w(700)/R_w(443)$ is 0.34. These ratios are similar to those at Sites 2, 3, and 4 at the visible wavelength. Generally, the average R_w at 443 nm was about 11% less than at 490 nm, 40% less than at 520 nm, 44% less than at 555 nm, 62% less than at 620 nm, and 69% less than at 700 nm. A similar trend for the changes in $R_w(\lambda)$ with increasing wavelength also occurred at 400 to 700 nm in the East China Sea study area. As a result, it was concluded that the reflectance decreased slowly with increasing wavelength when whitecaps appeared. These results indicate that the reflectance of whitecaps in the open ocean was dependent on wavelengths between 400 and 700 nm.

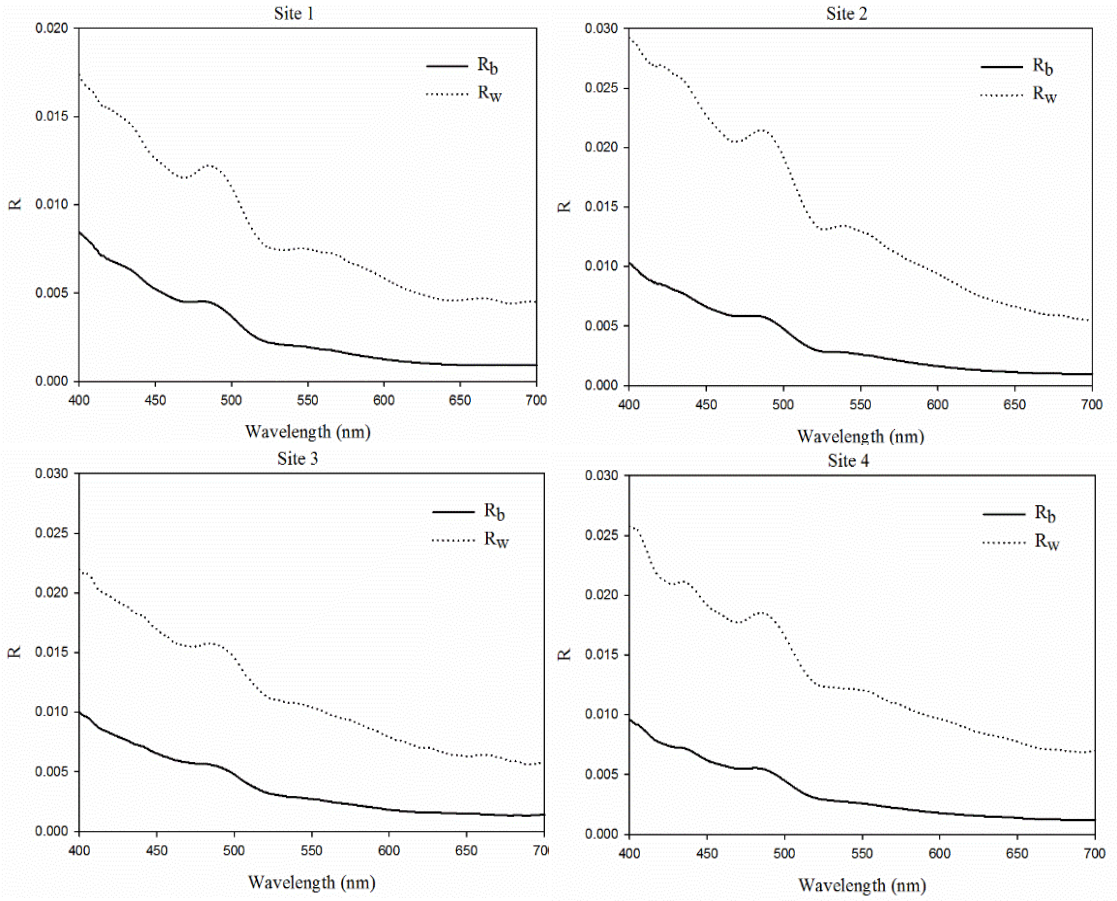

Figure 7. $R_b(\lambda)$ and $R_w(\lambda, U)$ at sites (1–4). (Solid line = $R_b(\lambda)$; broken line = $R_w(\lambda, U)$).

Table 4. Reflectance at 490, 520, 555, 620, and 700 nm divided by that at 443 nm. Generally, R_w at 443 nm is reduced by 88% at 490 nm, 67% at 520 nm, 63% at 555 nm, 51% at 620 nm and 46% at 700 nm.

Site	R_w	490/443	520/443	555/443	620/443	700/443
1	R_w	0.90	0.59	0.55	0.38	0.34
2	R_w	0.88	0.56	0.53	0.33	0.23
3	R_w	0.88	0.64	0.57	0.39	0.32
4	R_w	0.90	0.62	0.59	0.43	0.34

3.3. Variation of $\rho(\lambda, U)$ at Different Wind Speeds

The $\rho(\lambda, U)$ can be obtained by substituting the weighted average whitecap reflectance $R_w(\lambda, U)$ and the reflectance of background water $R_b(\lambda)$ into Equation (3). Figure 8 is a plot of $\rho(\lambda, U)$, shown to increase with increasing wavelength. The spectra are similar except at Site 8 (Figure 9). It was supposed that this large discrepancy may have been caused by the hull of the ship. During the observation period, the ship tended to yaw considerably. The sky condition at Site 8 was recorded as "some clouds", which suggests that the ship's shadow may have influenced the observed light field. Figure 8a shows that $\rho(\lambda, U)$ increased sharply when the wavelength increased from 400 to 620 nm, then increased slowly and began to decrease at 620–800 nm.

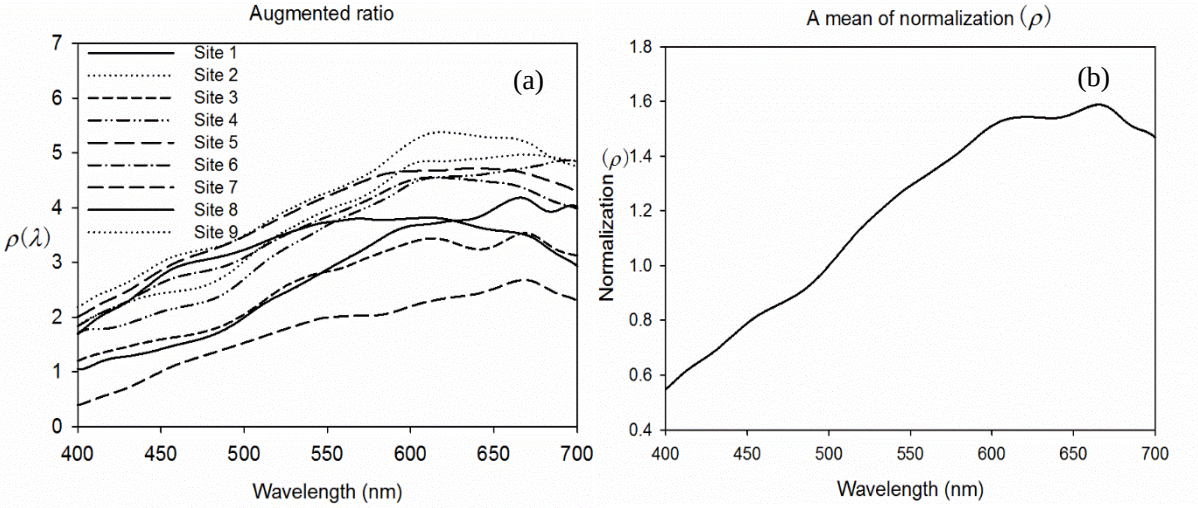

Figure 8. (**a**) $\rho(\lambda, U)$ *vs.* increasing wavelength from 400 to 700 nm. The spectra are similar except Site 8. When wind speed increased, generally ρ also increased. (**b**) Average $\rho(\lambda)/\rho(500)$ for the nine sites.

To predict $A(\lambda, U)$, it is necessary to know the relationship between $\rho(\lambda)$ and U_{10}. In a study of whitecap coverage in extreme hurricanes by Holthuijsen *et al.* [3], it was reported that the coverage approximated to a power law when $U_{10} \leq 24$ m·s^{-1}, and was constant when $U_{10} > 24$ m·s^{-1}. Since Equation (10) was used to describe w for values of $U_{10} > 9.25$ m·s^{-1}, wind speeds of 9.25 and 24 m·s^{-1} were set as the bounds of the augmented ratio. In the present study, data from the nine sites was used to study the relationship between measured $\rho(\lambda)$ and U_{10} (these include the study areas in the South China Sea and the East China Sea). Two processes were conducted on $\rho(\lambda)$. First, all the $\rho(\lambda)$ were normalized with $\rho(500)$. Second, by averaging the normalization $\rho(\lambda)$ at the nine sites, a mean $\rho(\lambda)$ was obtained as shown in Figure 8. The median wavelength of 500 nm was chosen and a fit equation was obtained to describe the relationship between $\rho(\lambda)$ and U_{10}:

$$\rho_{simulated}(500) = -283.3U_{10}^{-2.2} + 4 \quad (11)$$

Figure 9c shows the measured and simulated $\rho(500)$. To obtain values of $\rho(\lambda)$ in the visible spectrum, an average $\rho(\lambda)/\rho(500)$ was adopted, giving the simulated relationship

$$\rho_{simulated}(\lambda) = \frac{\rho(\lambda)}{\rho(500)}\rho_{simulated}(500) = \frac{\rho(\lambda)}{\rho(500)}(-283.3U_{10}^{-2.2} + 4) \quad (12)$$

where $\rho(\lambda)/\rho(500)$ is obtained from Figure 8b. For example, λ = 400 nm gives the ratio $\rho(400)/\rho(500)$ = 0.55; therefore $\rho_{simulated}(\lambda)$ is $\rho_{simulated}(400) = 0.55(-283.3U_{10}^{-2.2} + 4)$. The results for 400, 500, 600, and 700 nm are shown in Figure 9a, b, c and d, respectively. The values of R^2 and RMSE indicate that Equation (12) gives a reasonable estimate of $\rho(\lambda)$. Generally, $\rho(\lambda)$ increases sharply with increasing wind speed from 9.25 to 14 m·s^{-1} then begins to increase more slowly, even approaching a constant value with increasing wind speed.

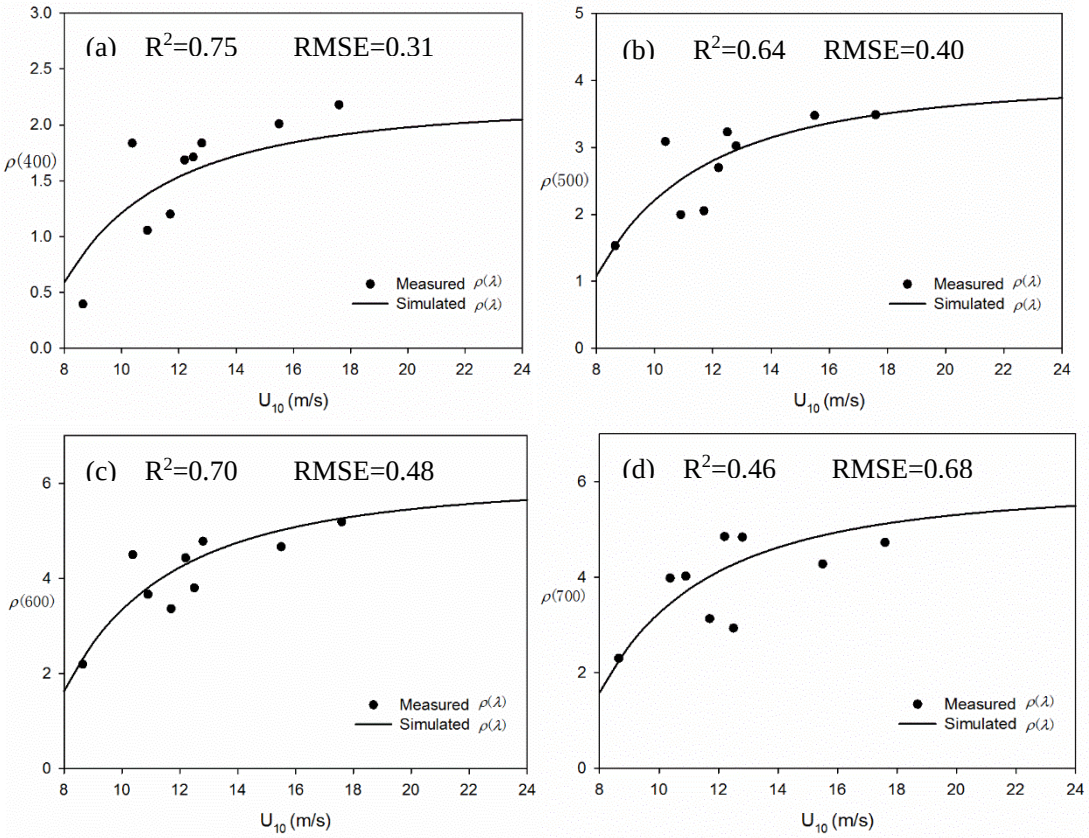

Figure 9. Measured and simulated $\rho(\lambda)$ at 400, 500, 600, and 700 nm were given in (**a**–**d**), respectively.

4. Discussion

Once $w(U)$ and $\rho(\lambda, U)$ had been obtained as described above, then $A(\lambda, U)$ could be calculated using Equation (5). The result can be stated as

$$A(\lambda, U) = w(U)\rho(\lambda, U) = 4.82 \times 10^{-6}\frac{\rho(\lambda)}{\rho(500)}(U_{10} + 1.98)^3(-283.3U_{10}^{-2.2} + 4) \quad (13)$$

At wavelengths from 400 to 700 nm, $A(\lambda, U)$ is obtained by substituting U and the average value of $\rho(\lambda)/\rho(500)$ from Figure 8b into Equation (13). The model proposed by Callaghan *et al.* [28] was adopted here to estimate w at $U_{10} > 9.25$ m·s^{-1}. Furthermore, w increases with increasing U_{10} following a power law, and then takes a constant value of 0.04 at $U_{10} > 24$ m·s^{-1} [3]. Equation (13) was thus used within the wind speed range of 9.25 to 24 m·s^{-1}.

In 2000, Moore used a radiometric system to study remote sensing augmented reflectance (RSAR) in the presence of breaking waves [19]. The instrument consisted of a six-channel radiometer centered at 410, 440, 510, 550, 670, and 860 nm. Moore *et al.* used the law expressed in the Monahan and Muircheartaigh [34] model (for stable $\Delta T = 2$) to relate RSAR to U using the measurements. Then they established a model, RSAR(412) $=3.4 \times 10^{-6}U^{2.55}$, with results given in Figure 10. They found that RSAR was essentially independent of wavelength and in the range 0.001–0.002 for wind speeds of 9–12 m·s^{-1}. Furthermore, the Koepke whitecap reflectance model converted to augmented reflectance, RSAR $= 4.57 \times 10^{-7}U^{3.52}$, was given in solid line in Figure 11. In this study, $\mathrm{RSAR}(\lambda, \mathrm{U})$ is different from $\mathrm{A}(\lambda, \mathrm{U})$ but they are related as:

$$\mathrm{RSAR}(\lambda, \mathrm{U}) = \mathrm{A}(\lambda, \mathrm{U})R_b(\lambda) \tag{14}$$

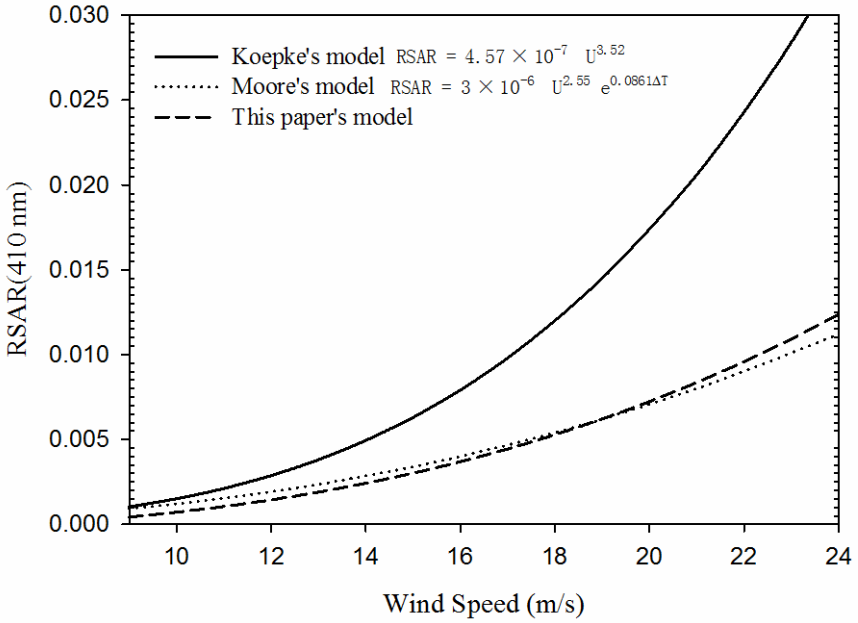

Figure 10. Predicted remote sensing augmented reflectance (RSAR) at 410 nm using three kinds of models. The solid line is the Koepke whitecap reflectance model [25] converted to augmented reflectance, RSAR $= 4.57 \times 10^{-7}U^{3.52}$. The dotted line is the Moore model [19], RSAR $=3.4 \times 10^{-6}U^{2.55}$. The broken line is the product of $\mathrm{A}(\lambda)$ obtained using proposed Equation (13) and 0.065 (the value of $\mathrm{R_b}(410)$) obtained by Moore *et al.* [19].

In the measurements reported by Moore *et al.* [19], $\mathrm{R_b}(\lambda)$ was approximately 0.065 at 410 nm. Therefore, the value of $\mathrm{RSAR}(410)$ was calculated from Equations (13) and (14). Figure 10 shows the values of $\mathrm{RSAR}(410)$ estimated by the different models. At $U_{10} = 14$ m·s^{-1}, $\mathrm{RSAR}(410)$ was 0.0015 obtained from Koepke's model, 0.0012 from Moore *et al.*'s model, and 0.0007 in the present proposed model. As the wind speed increased, the difference in $\mathrm{RSAR}(410)$ between Koepke's model and our model increased, whereas the discrepancy between Moore *et al.*'s model and our model decreased with increasing wind speed at $U_{10} < 19.5$ m·s^{-1}. The uncertainty in the values of effective reflectance and the efficiency factor are relatively high in Koepke's model as a result of their use of data obtained under different observed conditions, including differences in the seawater components, sky condition, sea wave and solar glitter. The uncertainty in the value of w adopted in Koepke's paper was also relatively high since it referred to different authors, and because of the wide variation of the data and the subjective

judgement in the analysis. The errors in both w and reflectance introduced a large overall uncertainty in Koepke's estimated $\mathrm{RSAR}(410)$. The effective reflectance errors did not appear in Moore *et al.*'s experiment since all the data was directly observed *in situ*. The dotted line in Figure 10 shows their result. The discrepancy between Moore *et al.*'s model and the present model increases either side of a wind speed of about 19 m·s^{-1}. The RSAR calculated using our model is greater than that calculated from Moore's model, which was developed from *in situ* wind speed measurements in the range 9 to 12 m·s^{-1}, whereas our experiments were conducted at wind speeds from 8.6 to 17.6 m·s^{-1}. As pointed out above, $\rho(\lambda)$ increases sharply wind speed increases from 9.25 to 14 m·s^{-1}, then the rate of increase begins to slow and approaches a constant value at higher wind speeds, such that the proposed $\rho(\lambda)$ caused the $\mathrm{RSAR}(410)$ discrepancy to decrease before $U_{10} < 19.5$ m·s^{-1}, then increase after $U_{10} > 19.5$ m·s^{-1}. However, the present proposed model is reasonably consistent with Moore *et al.*'s result. Because of the parameter $\rho(\lambda)$ introduced in this work, it is suggested that the model proposed here is more suitable than existing models for estimating $\mathrm{A}(\lambda)$ when $U_{10} > 14$ m·s^{-1}.

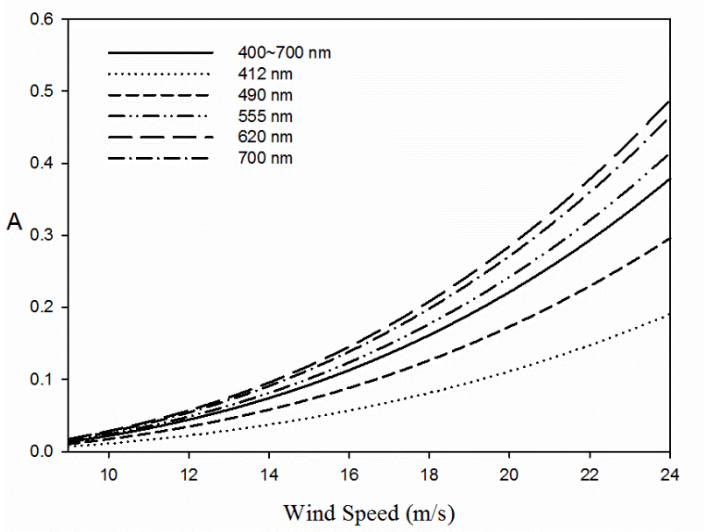

Figure 11. Change in $\mathrm{A}(\lambda, \mathrm{U})$ with increasing wind speed at wavelengths 412, 490, 555, 620 and 700 nm. The average value for the range 400–700 nm is also shown.

As shown in Figure 11, at the visible wavelengths, the averaged $\mathrm{A}(\lambda, \mathrm{U})$ given by $(\mathrm{A}(400, \mathrm{U}) + \mathrm{A}(401, \mathrm{U}) + \cdots + \mathrm{A}(700, \mathrm{U}))/301)$ is approximately 1.3% when U = 9 m·s^{-1} and w = 0.006; 2.2% when U = 10 m·s^{-1} and w = 0.008; 4.4% when U = 12 m·s^{-1} and w = 0.013; 7.4% when U = 14 m·s^{-1} and w = 0.020; 19% when U = 19 m·s^{-1} and w = 0.045; and 37.9% when U = 24 m·s^{-1} and w = 0.085 m·s^{-1}. It is then necessary to consider the augmented reflectance ratio for remote sensing applications. Note that RSAR is not the best parameter for describing this when whitecaps appear on the sea surface. Generally, seawater is optically assumed to comprise pure seawater, suspended particulate, and colored, dissolved organic matter. These components tend to be temporally and spatially variable. This occurred in the present case, as Figure 3 shows. Previous models had assumed that the reflectance of background seawater was constant, as discussed above. Using RSAR to describe the augmented reflectance ratio introduces a large error, since background seawater reflectance varies considerably. Thus, to describe the augmented reflectance ratio for ocean seawater, the parameter $\mathrm{R_b}(\lambda)$ was introduced into the model. In the present study, $\rho(\lambda, \mathrm{U})$ is a significant parameter that establishes a relationship between $\mathrm{R_b}(\lambda)$

and $R_w(\lambda)$. It is suggested that the proposed model $A(\lambda, U) = w(U)\rho(\lambda, U)$ rigorously takes account of the reflectance error for ocean seawater when whitecaps appear.

5. Conclusions

The earlier models for estimating the augmented reflectance on the sea surface when whitecaps appear had assumed that the reflectance of background seawater is constant. In fact, it tends to be more temporally and spatially variable than was first thought. As a result, the earlier models were highly uncertain when the background seawater reflectance changed. In the present work, a model is proposed for estimating the augmented reflectance ratio ($A(\lambda, U)$) for different fractional coverage of whitecaps (w). The augmented ratio of the reflectance of background water $\rho(\lambda, U)$ and w are the crucial parameters in the proposed model. Using a specifically designed whitecap measurement system, whitecap reflectance measurements were conducted in the South China Sea and East China Sea, and the derived data was analyzed by a band ratio method to obtain w. The results showed that the Callaghan *et al.* [28] empirical equation was suitable for obtaining w in the study region. $\rho(\lambda, U)$ was derived after determining the probability distribution function for whitecap reflectance. An exponential equation was established to describe the relationship between $\rho(\lambda, U)$ and U. Finally, $A(\lambda, U)$ was obtained and given as $A(\lambda, U) = 4.82 \times 10^{-6} \frac{\rho(\lambda)}{\rho(500)} (U_{10} + 1.98)^3 (-283.3 U_{10}^{-2.2} + 4)$. Estimating RSAR using $A(\lambda, U)$ and $R_b(\lambda)$ showed that $RSAR(\lambda, U)$ was in reasonably good agreement with earlier studies at wind speeds from 9 to 12 m·s^{-1}, which confirmed that the model is credible. Generally, our results showed that $A(400\sim700, U)$ is approximately 1.3% when U = 9 m·s^{-1} and w = 0.006; 2.2% when U = 10 m·s^{-1} and w = 0.008; 4.4% when U = 12 m·s^{-1} and w = 0.013; 7.4% when U = 14 m·s^{-1} and w = 0.020; 19% when U = 19 m·s^{-1} and w = 0.045; and 37.9% when U = 24 m·s^{-1} and w = 0.085 m·s^{-1}. Because the reflectance of background seawater has been taken into account in this model, $A(\lambda, U) = w(U)\rho(\lambda, U)$ gives a more scientifically rigorous method of determining the reflectance error when whitecaps appear.

Acknowledgements

This study was supported by the Youth Foundation of the State Key Laboratory of Tropical Oceanography (Grant No. SQ201102) and the Natural Science for Youth Foundation (Grant Nos. 41206029, 41406205, and 41206165). We express our appreciation to many colleagues in our group, who supported this field campaign. The data was provided by Zhantang Xu (email: xujiantang@163.com).

Author Contributions

Zhantang Xu and Zhaohua Sun proposed the core idea of the observation method and designed the framework of the paper; Zhantang Xu performed the data analysis and manuscript writing; Yuezhong Yang and Wenxi Cao designed and provided the observation instrument; Wen Zhou, Junfang Lin, Guifen Wang, Qian Yang and Zhantang Xu observed the data *in situ*.

Conflicts of Interest

The author declares no conflict of interest.

References

1. Gordon, H.R.; Wang, M. Influence of oceanic whitecaps on atmospheric correction of ocean-color sensors. *Appl. Opt.* **1994**, *33*, 7754–7763.
2. Frouin, R.; Schwindling, M.; Deschamps, P.Y. Spectral reflectance of sea foam in the visible and near-infrared: In situ measurements and remote sensing implications. *J. Geophys. Res. Ocean.* **1996**, *101*, 14361–14371.
3. Holthuijsen, L.H.; Powell, M.D.; Pietrzak, J.D. Wind and waves in extreme hurricanes. *J. Geophys. Res. Ocean.* **2012**, *117*, 45–57.
4. Frouin, R.; Iacobellis, S.; Deschamps, P.Y. Influence of oceanic whitecaps on the global radiation budget. *Geophys. Res. Lett.* **2001**, *28*, 1523–1526.
5. Kokhanovsky, A.A. Spectral reflectance of whitecaps. *J. Geophys. Res. Ocean.* **2004**, *109*, 285–288.
6. Salisbury, D.J.; Anguelova, M.D.; Brooks, I.M. Global distribution and seasonal dependence of satellite-based whitecap fraction. *Geophys. Res. Lett.* **2014**, *41*, 1616–1623.
7. Gordon, H.R.; Wang, M. Retrieval of water-leaving radiance and aerosol optical thickness over the oceans with seawifs: A preliminary algorithm. *Appl. Opt.* **1994**, *33*, 443–452.
8. Moore, K.D.; Voss, K.J.; Gordon, H.R. Spectral reflectance of whitecaps: Instrumentation, calibration, and performance in coastal waters. *J. Atmos. Ocean. Technol.* **1998**, *15*, 496–509.
9. Cunningham, A.; Boyle, J.C.; Wood, P. Radiative transfer modelling of the relationship between seawater composition and remote sensing reflectance in sea lochs and fjords. *Int. J. Remote Sens.* **2002**, *23*, 3713–3724.
10. Payne, R.E. Albedo of the sea surface. *J. Atmos. Sci.* **1972**, *29*, 959–970.
11. Maul, G.A.; Gordon, H.R. On the use of the earth resources technology satellite (Landsat-1) in optical oceanography. *Remote Sens. Environ.* **1976**, *4*, 95–128.
12. Gordon, H.R.; Jacobs, M.M. Albedo of the ocean-atmosphere system: Influence of sea foam. *Appl. Opt.* **1977**, *16*, 2257–2260.
13. Whitlock, C.H.; Bartlett, D.S.; Gurganus, E.A. Sea foam reflectance and influence on optimum wavelength for remote sensing of ocean aerosols. *Geophys. Res. Lett.* **1982**, *9*, 719–722.
14. Allison, D.B.; Stramski, D.; Mitchell, B.G. Empirical ocean color algorithms for estimating particulate organic carbon in the southern ocean. *J. Geophys. Res. Ocean.* **2010**, *115*, 1971–1982.
15. Hu, C.M.; Chen, Z.Q.; Clayton, T.D.; Swarzenski, P.; Brock, J.C.; Muller-Karger, F.E. Assessment of estuarine water-quality indicators using MODIS medium-resolution bands: Initial results from Tampa Bay, FL. *Remote Sens. Environ.* **2005**, *94*, 425–427.
16. Coble, P.; Hu, C.; Gould, R.W., Jr; Chang, G.; Wood, A.M. *Colored Dissolved Organic Matter in the Coastal Ocean An Optical Tool for Coastal Zone Environmental Assessment & Management*; Naval Research Lab, Stennis Space Center, MS. Oceanography Div.: Arlington, VA, USA, 2004.
17. Zhao, J.; Barnes, B.; Melo, N.; English, D.; Lapointe, B.; Muller-Karger, F.; Schaeffer, B.; Hu, C. Assessment of satellite-derived diffuse attenuation coefficients and euphotic depths in South Florida coastal waters. *Remote Sens. Environ.* **2013**, *131*, 38–50.
18. Wang, M.; Son, S.; Harding, L.W. Retrieval of diffuse attenuation coefficient in the Chesapeake Bay and turbid ocean regions for satellite ocean color applications. *J.Geophys. Res. Ocean.* **2009**, *114*, 244–254.

19. Moore, K.D.; Voss, K.J.; Gordon, H.R. Spectral reflectance of whitecaps: Their contribution to water-leaving radiance. *J. Geophys. Res. Ocean.* **2000**, *105*, 6493–6499.
20. Carratelli, E.P.; Dentale, F.; Reale, F. Numerical simulation of whitecaps and foam effects on satellite altimeter response. *Remote Sens.* **2014**, *6*, 3681–3692.
21. Reul, N.; Chapron, B. A model of sea-foam thickness distribution for passive microwave remote sensing applications. *J. Geophys. Res. Ocean.* **2003**, *108*, C10.
22. Mobley, C.D. Estimation of the remote-sensing reflectance from above-surface measurements. *Appl. Opt.* **1999**, *38*, 7442–7455.
23. Mobley, C.D. *Light and Water: Radiative Transfer in Natural Waters*; Academic Press: Manhattan, NY, USA, 1994.
24. Lee, Z.; Hu, C. Global distribution of Case-1 waters: An analysis from seawifs measurements. *Remote Sens. Environ.* **2006**, *101*, 270–276.
25. Koepke, P. Effective reflectance of oceanic whitecaps. *Appl. Opt.* **1984**, *23*, 1816–1824.
26. Bortkovskii, R.; Novak, V. Statistical dependencies of sea state characteristics on water temperature and wind-wave age. *J. Mar. Syst.* **1993**, *4*, 161–169.
27. Ross, D.B.; Cardone, V. Observations of oceanic whitecaps and their relation to remote measurements of surface wind speed. *J. Geophys. Res.* **1974**, *79*, 444–452.
28. Callaghan, A.; de Leeuw, G.; Cohen, L.; O'Dowd, C.D. Relationship of oceanic whitecap coverage to wind speed and wind history. *Geophys. Res. Lett.* **2008**, *35*, L23609.
29. Moat, B.I.; Yelland, M.; Pascal, R. Oceanic whitecap coverage measured during UK-SOLAS cruises. In Proceedigs of 16th Conference on Air-Sea Interaction, Phoenix, AZ, USA, 10–15 January 2009.
30. Zhao, D.; Toba, Y. Dependence of whitecap coverage on wind and wind-wave properties. *J. Oceanogr.* **2001**, *57*, 603–616.
31. Goddijn-Murphy, L.; Woolf, D.K.; Callaghan, A.H. Parameterizations and algorithms for oceanic whitecap coverage. *J. Phys. Oceanogr.* **2011**, *41*, 742–756.
32. Anguelova, M.D.; Webster, F. Whitecap coverage from satellite measurements: A first step toward modeling the variability of oceanic whitecaps. *J. Geophys. Res.Ocean.* **2006**, *111*, C3.
33. Sugihara, Y.; Tsumori, H.; Ohga, T.; Yoshioka, H.; Serizawa, S. Variation of whitecap coverage with wave-field conditions. *J. Mar. Syst.* **2007**, *66*, 47–60.
34. Monahan, E.C.; Muircheartaigh, I. Optimal power-law description of oceanic whitecap coverage dependence on wind speed. *J. Phys. Oceanogr.* **1980**, *10*, 2094–2099.